A Geometry-Based Underwater Acoustic Channel Model Allowing for Sloped Ocean Bottom Conditions

Meisam Naderi, *Student Member, IEEE*, Matthias Pätzold, *Senior Member, IEEE*, Rym Hicheri, and Néji Youssef

Abstract—This paper proposes a new geometry-based channel model for shallow-water ocean environments in which the ocean bottom can slope gently down/up. The need for developing such an underwater acoustic (UWA) channel model is driven by the fact that the standard assumption of a flat ocean bottom does not hold in many realistic scenarios. Starting from a geometrical model, we develop a stochastic channel model for wideband single-input single-output vehicle-to-vehicle UWA channels using the ray theory assuming smooth ocean surface and bottom. We investigate the effect of the ocean-bottom slope angle on the distribution of the channel envelope, instantaneous channel capacity, temporal autocorrelation function, frequency correlation function, Doppler power spectral density, and the power delay profile. Theoretical and simulation results show that even a relatively small slope angle influences considerably the statistical properties of UWA channels. The validation of the proposed UWA channel model has been performed by fitting its main characteristic quantities (average delay, delay spread, and coherence bandwidth) to measurement data. In comparison with the conventional UWA channel model, which has been developed on the assumption of a flat ocean bottom, it is shown that the proposed UWA channel model enables the modelling of measured channels with higher precision.

Index terms — Shallow underwater acoustic channels, instantaneous channel capacity, Doppler power spectral density, power delay profile, temporal correlation function.

I. INTRODUCTION

In recent years, underwater acoustic (UWA) communication systems have received considerable attention. UWA networks have been studied in various areas due to their potential applications in oceanography that involve the exploration of the ocean [1], support for underwater robots [2], offshore oil industry exploration [3], and pollution monitoring [4], just to name a few examples. Owing to the fact that electromagnetic waves and laser beams suffer from high path loss in ocean water, acoustic signals are being used, especially, in medium- and long-range underwater communications. For the design, test, and performance analysis of UWA communication systems, realistic channel models are required. This calls for the statistical analysis of UWA channels in terms of the channel envelope distribution, instantaneous channel capacity,

M. Naderi and M. Pätzold are with the Faculty of Engineering and Science, University of Agder, 4887 Grimstad, Norway (e-mails: {meisam.naderi, matthias.paetzold}@uia.no).

R. Hicheri and N. Youssef are with the Ecole Supérieure des Communications de Tunis, Ariana 2083, Tunisia (e-mails: {rym.hicheri@supcom.tn, neji.youssef@supcom.rnu.tn).

correlation functions, Doppler power spectral density (PSD), and power delay profile (PDP).

UWA wave propagation in the ocean is described by the wave equation, but the development of a proper propagation model by solving the wave equation is well known to be a difficult problem [5]. To circumvent this problem, approximations by means of the ray theory are often used to model the acoustic wave propagation phenomena in ocean environments [6]. By invoking the ray theory, the energy of sound propagates in shallow-water environments along straight lines like light rays, where the speed of sound is assumed to be constant (isovelocity assumption) [5], [7], [8].

Moreover, several stochastic channel models have been developed for UWA communication systems under the assumption that the ocean bottom is flat [5], [9]–[13]. For example, in [5] and [9], the total distances that *macro-eigenrays* travel between the transmitter and the receiver have been computed by using the *method of image projections*, which has first been introduced in [6]. In both aforementioned papers, the reference channel models have been developed by combining the deterministic ray-tracing concept with statistical methods to account for the randomness of the propagation environment. However, the ocean bottom is not necessarily flat and most parts of the ocean bottom slope gradually from the shore to the high and deep ocean. This natural feature motivated us to develop a new geometrical model which we call the sloped-ocean-bottom (SOB) model. The objective of this paper is to start from the geometrical SOB model and to develop a general stochastic UWA channel model that accounts for SOB conditions. It is shown that the flat-ocean-bottom (FOB) model, which is widely used in the literature [5], [9]–[13], can be obtained as a special case of the proposed model if the slope angle is zero.

In this context, several studies have been conducted to investigate the probability density functions (PDFs) of the UWA channel gains and the corresponding instantaneous capacity [14]–[16]. The study of these statistical characteristics is of great importance as it allows us to gain a deeper insight into the dynamical and temporal behavior of UWA channels.

In this paper, we develop a geometry-based UWA channel model assuming ray propagation in shallow-water ocean environments by taking *macro-scattering* effects, which are caused by specular reflections at the surface and bottom of the ocean, into account. The randomness of the UWA channel as a result of *micro-scattering* (diffuse scattering) effects will not be discussed in this paper. Starting from the geometrical SOB

model, we derive the time-variant channel impulse response (TVCIR) of the UWA channel model. Expressions are derived for the total distances that the macro-eigenrays travel from the transmitter to the receiver by assuming multiple-bounce scattering in shallow-water environments. We also study the angles-of-departure (AODs) and the angles-of-arrival (AOAs) of the macro-eigenrays. Furthermore, we investigate the effect of the ocean-bottom slope angle on the PDF of the UWA channel envelope and the PDF of the instantaneous channel capacity. Moreover, the statistical quantities of the proposed SOB-UWA channel model, such as the temporal autocorrelation function (ACF), frequency correlation function (FCF), Doppler PSD, and the PDP, are compared with those of the FOB-UWA channel model. The influence of the slope angle on the Doppler spread, average Doppler shift, coherence time, average delay, delay spread, and the coherence bandwidth of the UWA channel model are also studied. It is shown that the ocean-bottom slope angle considerably influences the statistical properties of UWA channels. The key theoretical results are illustrated by computer simulations.

In addition, the main statistical properties of the proposed UWA channel model, such as the FCF, average delay, delay spread, and the coherence bandwidth have been matched to real-world measurement data of UWA channels. The observed excellent agreement between model prediction and experimental measurement confirms the validity of the proposed SOB-UWA model. Moreover, the superiority of the SOB model over the FOB model is shown regarding the modelling of characteristic quantities (such as the delay spread and coherence bandwidth) of the measurement data, which are useful quantities for designing UWA communication systems, especially when orthogonal frequency division multiplexing (OFDM) techniques are used.

The rest of this paper is organized as follows. In Section II, the geometrical UWA channel model is presented. Section III studies the stochastic UWA channel model from the geometrical UWA model. Section IV focuses on the statistical properties of the proposed UWA channel model. The numerical results are illustrated in Section V. The validation of the main theoretical results through measurement data is outlined in Section VI. Finally, the conclusions are drawn in Section VII.

II. THE GEOMETRICAL SOB-UWA MODEL

In this section, we present a new geometrical model for a wideband single-input single-output (SISO) shallow-water ocean environment under the assumption that the ocean surface and ocean bottom are smooth. In addition, it is assumed that the ocean bottom declines (inclines) with a slope angle denoted by ϕ. The shallow-water ocean environment is considered as an isovelocity environment. This paper considers medium- and long-range shallow UWA communication links under line-of-sight (LOS) propagation conditions. The UWA channel is also assumed to be wide-sense stationary in time and frequency.

Fig. 1 presents the geometrical model of a SOB-UWA channel in a shallow-water ocean environment. As can be seen, the two-dimensional geometrical SOB model is bounded by the ocean surface and bottom. These natural boundaries act as reflectors for acoustic waves such that several macro-eigenrays can travel from the transmitter T_x to the receiver R_x. With reference to Fig. 1, there are three kinds of macro-eigenrays. They can be grouped into downward arriving (DA) macro-eigenrays, upward arriving (UA) macro-eigenrays, and a LOS macro-eigenray. Each of the DA macro-eigenrays for which the last reflection originates from the ocean surface can have a different number of s surface reflections and $\breve{b}$ bottom reflections. Let N_S be the maximum number of surface interactions that a DA macro-eigenray can have with the ocean surface, then s and $\breve{b}$ are limited by $1 \leq s \leq N_S$ and $s - 1 \leq \breve{b} \leq s$, respectively. At any time instance t, the receiver R_x receives $2N_S$ DA macro-eigenrays. The UA macro-eigenrays for which the last reflection originates from the ocean bottom can have a different number of b bottom reflections and $\breve{s}$ surface reflections. Analogously, let N_B denote the maximum number of bottom interactions that a UA macro-eigenray can have with the ocean bottom, then b and $\breve{s}$ are limited by $1 \leq b \leq N_B$ and $b - 1 \leq \breve{s} \leq b$, respectively. Similarly, at the time instance t, the receiver R_x receives $2N_B$ UA macro-eigenrays. For instance, if a UA macro-eigenray has only one interaction with the ocean bottom, i.e., $N_B = 1$, then there are two possible paths which this macro-eigenray can travel from the transmitter T_x to the receiver R_x. The first path arrives at R_x after a single bounce on the bottom of the ocean, i.e., $b = 1$, and $\breve{s} = 0$. The second path is a double-bounce path if a UA macro-eigenray starts upward. This means the macro-eigenray first interacts with the ocean surface and then, after interacting with the ocean bottom, arrives at R_x, i.e., $b = 1$ and $\breve{s} = 1$. It should be mentioned that experimental results obtained for medium- and long-range shallow UWA channels have shown that the number of macro-eigenrays arriving at R_x rarely exceeds 8, i.e., $2N_S + 2N_B = 8$ [5], [9], [17], [18].

The exact positions of the *macro-scatterers* are computable and depend on the waveguide geometry and the number of macro-eigenrays [6]. In [6], the total distances which macro-eigenrays travel in FOB models after their interactions with macro-scatterers, located at the ocean surface and bottom, have been derived by using the method of images. *Micro-scatterers*, which can be clustered around the positions of macro-scatterers will not be considered in our paper. In other words, we limit our study to the propagation of deterministic macro-eigenrays by considering only the specular (mirror-like) reflections of the ocean surface and bottom.

Moreover, we assume that the transmitter T_x and the receiver R_x are moving with velocities $\vec{v}_T$ and $\vec{v}_R$ in the directions determined by the angles-of-motion (AOMs) α_v^T and α_v^R, respectively. As shown in Figs. 1 and 2, the transmitter T_x (receiver R_x) is located at the distances y_1^T (y_1^R) and y_2^T (y_2^R) from the ocean surface and ocean bottom, respectively. The distance along the x-axis between T_x and R_x is denoted by D. As can be seen in Fig. 2, the symbol $\beta_{s\breve{b}}^{DA}$ ($\alpha_{s\breve{b}}^{DA}$) stands for the AODs (AOAs) of the DA macro-eigenrays associated with the number of surface interactions s and bottom interactions $\breve{b}$. Analogously, the symbol $\beta_{b\breve{s}}^{UA}$ ($\alpha_{b\breve{s}}^{UA}$) also denotes the AODs (AOAs) of UA macro-eigenrays associated with the number of bottom interactions b and surface interactions $\breve{s}$. The symbol
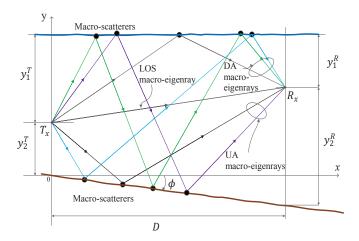
Fig. 1. Illustration of the LOS macro-eigenray and several DA and UA macro-eigenrays which travel from T_x to R_x in a shallow UWA channel ($N_S = 2$, $N_B = 1$).
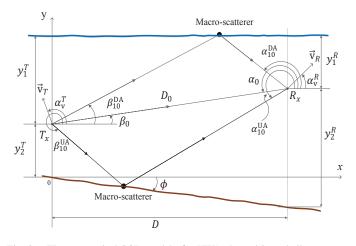

Fig. 2. The geometrical SOB model of a UWA channel in a shallow-water ocean environment.

β_0 (α_0) stands for the AOD (AOA) of the LOS component.

III. THE GEOMETRY-BASED SOB-UWA CHANNEL MODEL

In this section, we develop a mathematical model for the macro-eigenray propagation through shallow-water environments, where it is assumed that the ocean bottom slopes down or up. We first present the TVCIR of the proposed geometry-based channel model for a vehicle-to-vehicle (V2V) UWA wideband fading channel under LOS propagation conditions. Then, we drive the expressions of the total distances which macro-eigenrays travel from T_x to R_x after their interactions with the surface and bottom of the ocean. The AODs and the AOAs, which are required for computing the Doppler frequencies, are also studied. We show that the proposed UWA channel model includes the well-known model in [9], where the ocean bottom is flat, as a special case.

A. TVCIR

According to the geometrical model shown in Fig. 2, the TVCIR $h(\tau', t)$ can be split into three parts. The first part

$h^{\mathrm{LOS}}(\tau', t)$ describes the LOS component, whereas the second part $h^{\mathrm{DA}}(\tau', t)$ and the third part $h^{\mathrm{UA}}(\tau', t)$ comprise the DA macro-eigenrays and the UA macro-eigenrays, respectively. Hence, the TVCIR $h(\tau', t)$ can be written as

$$h(\tau', t) = h^{\mathrm{LOS}}(\tau', t) + h^{\mathrm{DA}}(\tau', t) + h^{\mathrm{UA}}(\tau', t). \quad (1)$$

The LOS part $h^{\mathrm{LOS}}(\tau', t)$ of the TVCIR is described by the expression

$$h^{\mathrm{LOS}}(\tau', t) = c_0\, e^{j(2\pi f_0 t + \theta_0)} \delta(\tau' - \tau_0') \quad (2)$$

in which the gain c_0 is given by

$$c_0 = \sqrt{c_R/(1 + c_R)}\, A_s(D_0)\, A_a(D_0). \quad (3)$$

The parameter c_R is the Rice factor, and τ_0' denotes the propagation delay of the LOS component. The symbols f_0 and θ_0 represent the Doppler frequency and phase shift of the LOS component, respectively. The Doppler frequency f_0 in (2) is defined by

$$f_0 = f_{\max}^T \cos(\beta_0 - \alpha_v^T) + f_{\max}^R \cos(\alpha_0 - \alpha_v^R) \quad (4)$$

where $f_{\max}^T$ ($f_{\max}^R$) denotes the maximum Doppler frequency associated with the transmitter T_x (receiver R_x), which is given by $f_{\max}^T = v_T f_c/c_s$ ($f_{\max}^R = v_R f_c/c_s$). Therein, $v_T = |\vec{v}_T|$ ($v_R = |\vec{v}_R|$) denotes the speed of the transmitter (receiver), f_c indicates the carrier frequency (in Hz), and c_s is the speed of sound in water, which is assumed to be 1500 m/s (isovelocity environment). With reference to Fig. 2, the AOD β_0 and the AOA α_0 of the LOS component can be computed by

$$\beta_0 = \arctan\left(\frac{y_1^T - y_1^R}{D}\right) \quad (5)$$

and

$$\alpha_0 = \pi + \beta_0 \quad (6)$$

respectively. The propagation delay τ_0' can be expressed by

$$\tau_0' = \frac{D_0}{c_s} \quad (7)$$

where the total distance D_0 between T_x and R_x is given by

$$D_0 = \sqrt{D^2 + (y_1^T - y_1^R)^2}. \quad (8)$$

The functions $A_s(\cdot)$ and $A_a(\cdot)$ introduced in the gain c_0 [see (3)] denote the propagation loss coefficients due to spherical spreading and absorbtion, respectively. We assume that the transmitter is equipped with an omnidirectional hydrophone, which generates spherical waveforms in the isovelocity environment. The propagation loss coefficient due to spherical spreading can be written as [19, Eq. (2.16)]

$$A_s(d) = \frac{1}{d} \quad (9)$$

where the variable d stands for the total propagation distance in meters. The absorption loss coefficient $A_a(\cdot)$ is given by [9, Eq. (4)]

$$A_a(d) = 10^{-\frac{d\beta}{20000}}. \quad (10)$$

In (10), which is suitable for carrier frequencies between 3 and 500 kHz, the parameter β (in dB/km) is computed as follows [6, Eq. (1.3.1)]

$$\beta = 8.68 \times 10^3 \left(\frac{S_a f_T f_c^2 A}{f_T^2 + f_c^2} + \frac{B f_c^2}{f_T} \right) \left(1 - 6.54 \times 10^{-4} P \right) \tag{11}$$

where $A = 2.34 \times 10^{-6}$ and $B = 3.38 \times 10^{-6}$. The symbol S_a denotes the salinity (in parts per thousand), f_c is the carrier frequency (in kHz), f_T is the relaxation frequency (in kHz) determined by $f_T = 21.9 \times 10^{6 - (1520/(T+273))}$, and the quantity T denotes the water temperature (in $^\circ$C). The symbol P stands for the hydrostatic pressure (in kg/cm^2), which is determined by $P = 1.01 \times (1 + 0.1h)$, where h denotes the water depth (in m).

The second part $h^{\text{DA}}(\tau', t)$ and the third part $h^{\text{UA}}(\tau', t)$ of the TVCIR $h(\tau', t)$ in (1) are given by

$$h^{\text{DA}}(\tau', t) = \sum_{s=1}^{N_S} \sum_{\breve{b}=s-1}^{s} c_{s\breve{b}}^{\text{DA}} e^{j(2\pi f_{s\breve{b}}^{\text{DA}} t + \theta_{s\breve{b}}^{\text{DA}})} \delta(\tau' - \tau_{s\breve{b}}'^{\text{DA}}) \tag{12}$$

and

$$h^{\text{UA}}(\tau', t) = \sum_{b=1}^{N_B} \sum_{\breve{s}=b-1}^{b} c_{b\breve{s}}^{\text{UA}} e^{j(2\pi f_{b\breve{s}}^{\text{UA}} t + \theta_{b\breve{s}}^{\text{UA}})} \delta(\tau' - \tau_{b\breve{s}}'^{\text{UA}}) \tag{13}$$

respectively. The gains $c_{s\breve{b}}^{\text{DA}}$ and $c_{b\breve{s}}^{\text{UA}}$ are expressed by

$$c_{s\breve{b}}^{\text{DA}} = \sqrt{\frac{\eta_S}{2N_S(1 + c_R)}} A_s(D_{s\breve{b}}^{\text{DA}}) A_a(D_{s\breve{b}}^{\text{DA}}) A_b(\varphi_{s\breve{b}}^{\text{DA}} + (2\breve{b} - 1)\phi)^{\breve{b}} \tag{14}$$

and

$$c_{b\breve{s}}^{\text{UA}} = \sqrt{\frac{\eta_B}{2N_B(1 + c_R)}} A_s(D_{b\breve{s}}^{\text{UA}}) A_a(D_{b\breve{s}}^{\text{UA}}) A_b(\varphi_{b\breve{s}}^{\text{UA}})^{(b-1)}$$
$$\times A_b(\varphi_{b\breve{s}}^{\text{UA}} + 2(b-1)\phi) \tag{15}$$

respectively. The propagation delays $\tau_{s\breve{b}}'^{\text{DA}}$ and $\tau_{b\breve{s}}'^{\text{UA}}$ are determined by $\tau_{s\breve{b}}'^{\text{DA}} = D_{s\breve{b}}^{\text{DA}}/c_s$ ($s = 1, 2, ..., N_S$ and $\breve{b} \in [s-1, s]$) and $\tau_{b\breve{s}}'^{\text{UA}} = D_{b\breve{s}}^{\text{UA}}/c_s$ ($b = 1, 2, ..., N_B$ and $\breve{s} \in [b-1, b]$), respectively. The symbols $D_{s\breve{b}}^{\text{DA}}$ and $D_{b\breve{s}}^{\text{UA}}$ denote the total distances which the DA and UA macro-eigenrays travel form T_x to R_x given $(s, \breve{b})$ and $(\breve{s}, b)$ surface-bottom interactions, respectively. It is shown in the Appendix that the total distances $D_{s\breve{b}}^{\text{DA}}$ and $D_{b\breve{s}}^{\text{UA}}$ can be computed by using the method of images which results in (16) and (17), respectively (see the bottom of this page). The functions $f^{\text{DA}}(\phi)$ $\left(f^{\text{UA}}(\phi) \right)$, $g^{\text{DA}}(\phi)$ $\left(g^{\text{UA}}(\phi) \right)$, and $h^{\text{DA}}(\phi)$ $\left(h^{\text{UA}}(\phi) \right)$ in (16) ((17)) are presented in the Appendix.
The symbols η_S in (14) and η_B in (15) are used to balance the contribution of the DA and UA macro-eigenrays to the total power of the UWA channel model, respectively, such

that $\eta_S + \eta_B = 1$. The phase shifts $\theta_{s\breve{b}}^{\text{DA}}$ in (12) and $\theta_{b\breve{s}}^{\text{UA}}$ in (13) are modelled by independent and identically distributed (i.i.d.) random variables, which are supposed to be uniformly distributed over the interval $(-\pi, \pi]$.

The function $A_b(\cdot)$ in (14) and (15) denotes the reflection coefficient due to the impedance mismatch between the ocean water and the ocean bed. It should be mentioned that the impedance mismatch between the ocean water and air causes the sea surface to be a very good reflector. If the sea surface is smooth, the reflection coefficient has a magnitude that is close to one but the phase shift is π radians, i.e., the reflection coefficient is close to -1 [5], [6], [20]. In the area of underwater acoustic channel modeling, the ocean bed is definitely the most complex boundary, exhibiting vastly different reflectivity characteristics in different geographical locations [21], [22]. The impedance mismatch between the ocean water and ocean bed causes the ocean bed to reflect some parts of an incident wave. For a smooth ocean bed, the reflection coefficient $A_b(\cdot)$ is given by [6, Eq. (3.1.12)]

$$A_b(\varphi) = \left| \frac{(\rho_1/\rho_s)\cos(\varphi) - \sqrt{(c_s/c_1)^2 - \sin^2(\varphi)}}{(\rho_1/\rho_s)\cos(\varphi) + \sqrt{(c_s/c_1)^2 - \sin^2(\varphi)}} \right| \tag{18}$$

where ρ_s (ρ_b) and c_s (c_b) stand for the density of the ocean water (ocean bed) and the speed of sound in the ocean water (ocean bed), respectively. The symbol φ in (18) denotes the angle-of-incidence (AOI) of the macro-eigenrays of the specular reflections at the ocean bottom.

B. Derivation of the AOD and AOA

In this section, we derive analytical expressions for the AODs $\beta_{s\breve{b}}^{\text{DA}}$ ($\beta_{b\breve{s}}^{\text{UA}}$) and the AOAs $\alpha_{s\breve{b}}^{\text{DA}}$ ($\alpha_{b\breve{s}}^{\text{UA}}$), which are necessary to compute the Doppler frequencies of the macro-eigenrays. The Doppler frequencies $f_{s\breve{b}}^{\text{DA}}$ and $f_{b\breve{s}}^{\text{UA}}$ presented in (12) and (13), respectively, can be computed by using (4), if we replace β_0 by $\beta_{s\breve{b}}^{\text{DA}}$ ($\beta_{b\breve{s}}^{\text{UA}}$) and α_0 by $\alpha_{s\breve{b}}^{\text{DA}}$ ($\alpha_{b\breve{s}}^{\text{UA}}$). Note that the slope angle ϕ influences in our model the AOIs at the ocean surface and bottom as shown in Figs. 3 and 4. This is in contrast for the FOB environment, where the AOIs at the ocean bottom are fixed for each macro-eigenray. With reference to Figs. 3 and 4, the general solutions for the AODs $\beta_{s\breve{b}}^{\text{DA}}$ and $\beta_{b\breve{s}}^{\text{UA}}$ can be obtained as

$$\beta_{s\breve{b}}^{\text{DA}} = \left(\breve{b} - s + \frac{3}{2} \right) \pi + (-1)^{(s-\breve{b})} \left(\varphi_{s\breve{b}}^{\text{DA}} + 2\breve{b}\phi \right) \tag{19}$$

and

$$\beta_{b\breve{s}}^{\text{UA}} = \left(b - \breve{s} + \frac{1}{2} \right) \pi - (-1)^{(b-\breve{s})} \left[\varphi_{b\breve{s}}^{\text{UA}} + (2b-1)\phi \right] \tag{20}$$

$$D_{s\breve{b}}^{\text{DA}} = \sqrt{(D - f^{\text{DA}}(\phi))^2 + ((2s-1)g^{\text{DA}}(\phi)y_1^T + 2\breve{b}h^{\text{DA}}(\phi)y_2^T + y_1^R)^2} \tag{16}$$

$$D_{b\breve{s}}^{\text{UA}} = \sqrt{(D/\cos(\phi) - f^{\text{UA}}(\phi))^2 + (2\breve{s}g^{\text{UA}}(\phi)y_1^T + (2b-1)h^{\text{UA}}(\phi)y_2^T + y_2^R \cos(\phi))^2} \tag{17}$$
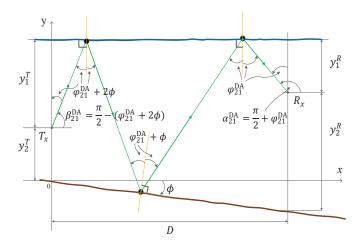
Fig. 3. The effect of the slope angle $\phi < 0$ on the AOIs $\varphi_{s\breve{b}}^{\text{DA}}$ of the DA macro-eigenray at the ocean surface/bottom for $s = 2$ and $\breve{b} = 1$.
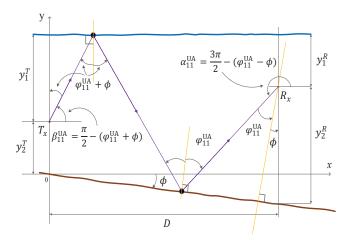

Fig. 4. The effect of the slope angle $\phi < 0$ on the AOIs $\varphi_{b\breve{s}}^{\text{UA}}$ of the UA macro-eigenray at the ocean surface/bottom for $b = \breve{s} = 1$.

respectively. Similarly, the general-form expressions for the AOAs $\alpha_{s\breve{b}}^{\text{DA}}$ and $\alpha_{b\breve{s}}^{\text{UA}}$ can be written as

$$\alpha_{s\breve{b}}^{\text{DA}} = \frac{\pi}{2} + \varphi_{s\breve{b}}^{\text{DA}} \tag{21}$$

and

$$\alpha_{b\breve{s}}^{\text{UA}} = \frac{3\pi}{2} - \left(\varphi_{b\breve{s}}^{\text{UA}} - \phi\right) \tag{22}$$

respectively. According to Figs. 3 and 4, the AOIs $\varphi_{s\breve{b}}^{\text{DA}}$ and $\varphi_{b\breve{s}}^{\text{UA}}$ at R_x play a key role in the determination of the AODs and AOAs presented in (19)–(22). The AOIs $\varphi_{s\breve{b}}^{\text{DA}}$ and $\varphi_{b\breve{s}}^{\text{UA}}$ can be expressed by

$$\varphi_{s\breve{b}}^{\text{DA}} = \arctan\left(\frac{D - f^{\text{DA}}(\phi)}{(2s-1)g^{\text{DA}}(\phi)y_1^T + 2\breve{b}h^{\text{DA}}(\phi)y_2^T + y_1^R}\right) \tag{23}$$

and

$$\varphi_{b\breve{s}}^{\text{UA}} = \arctan\left(\frac{D/\cos(\phi) - f^{\text{UA}}(\phi)}{2\breve{s}g^{\text{UA}}(\phi)y_1^T + (2b-1)h^{\text{UA}}(\phi)y_2^T + y_2^R\cos(\phi)}\right) \tag{24}$$

respectively. The proof of the expression in (23) is presented in the Appendix.

C. FOB Case

In this section, we will show that the proposed geometry-based SOB-UWA channel model includes the FOB-UWA model as a special case if $\phi = 0$. Recall that the FOB model has been widely used in the literature on UWA channel modelling [5], [9]–[13]. From now on, we underline the symbols, which are specific for the FOB model. The TVCIR $\underline{h}(\tau', t)$ in (1) will be written as

$$\underline{h}(\tau', t) = h^{\text{LOS}}(\tau', t) + \underline{h}^{\text{DA}}(\tau', t) + \underline{h}^{\text{UA}}(\tau', t) \tag{25}$$

where the first part $h^{\text{LOS}}(\tau', t)$ is the same as in (2), whereas the second part $\underline{h}^{\text{DA}}(\tau', t)$ and the third part $\underline{h}^{\text{UA}}(\tau', t)$ of $\underline{h}(\tau', t)$ are given by

$$\underline{h}^{\text{DA}}(\tau', t) = \sum_{s=1}^{N_S}\sum_{\breve{b}=s-1}^{s} \underline{c}_{s\breve{b}}^{\text{DA}}\, e^{j(2\pi \underline{f}_{s\breve{b}}^{\text{DA}}t + \theta_{s\breve{b}}^{\text{DA}})}\delta(\tau' - \underline{\tau}_{s\breve{b}}^{'\text{DA}}) \tag{26}$$

and

$$\underline{h}^{\text{UA}}(\tau', t) = \sum_{b=1}^{N_B}\sum_{\breve{s}=b-1}^{b} \underline{c}_{b\breve{s}}^{\text{UA}}\, e^{j(2\pi \underline{f}_{b\breve{s}}^{\text{UA}}t + \theta_{b\breve{s}}^{\text{UA}})}\delta(\tau' - \underline{\tau}_{b\breve{s}}^{'\text{UA}}) \tag{27}$$

respectively. The gains $\underline{c}_{s\breve{b}}^{\text{DA}}$ and $\underline{c}_{b\breve{s}}^{\text{UA}}$ can be expressed by

$$\underline{c}_{s\breve{b}}^{\text{DA}} = \sqrt{\frac{\eta_S}{2N_S(1+c_R)}}\, A_s(\underline{D}_{s\breve{b}}^{\text{DA}})A_a(\underline{D}_{s\breve{b}}^{\text{DA}})A_b(\underline{\varphi}_{s\breve{b}}^{\text{DA}})^{\breve{b}} \tag{28}$$

and

$$\underline{c}_{b\breve{s}}^{\text{UA}} = \sqrt{\frac{\eta_B}{2N_B(1+c_R)}}\, A_s(\underline{D}_{b\breve{s}}^{\text{UA}})A_a(\underline{D}_{b\breve{s}}^{\text{UA}})A_b(\underline{\varphi}_{b\breve{s}}^{\text{UA}})^{b} \tag{29}$$

respectively. The phase shifts $\theta_{s\breve{b}}^{\text{DA}}$ and $\theta_{b\breve{s}}^{\text{UA}}$ are again modelled by i.i.d. random variables, which are uniformly distributed over the interval $(-\pi, \pi]$. For $\phi = 0$, the total distances $\underline{D}_{s\breve{b}}^{\text{DA}}$ and $\underline{D}_{b\breve{s}}^{\text{UA}}$ in (16) and (17), respectively reduce to that in [6, Eq. (5.1.7)], namely

$$\underline{D}_{s\breve{b}}^{\text{DA}} = \sqrt{D^2 + ((2s-1)y_1^T + 2\breve{b}y_2^T + y_1^R)^2} \tag{30}$$

$$\underline{D}_{b\breve{s}}^{\text{UA}} = \sqrt{D^2 + (2\breve{s}y_1^T + (2b-1)y_2^T + y_2^R)^2}. \tag{31}$$

The propagation delays $\underline{\tau}_{s\breve{b}}^{'\text{DA}}$ in (26) and $\underline{\tau}_{b\breve{s}}^{'\text{UA}}$ in (27) can be computed by $\underline{\tau}_{s\breve{b}}^{'\text{DA}} = \underline{D}_{s\breve{b}}^{\text{DA}}/c_s$ ($s = 1, 2, ..., N_S$ and $\breve{b} \in [s-1, s]$) and $\underline{\tau}_{b\breve{s}}^{'\text{UA}} = \underline{D}_{b\breve{s}}^{\text{UA}}/c_s$ ($b = 1, 2, ..., N_B$ and $\breve{s} \in [b-1, b]$), respectively. Similar to Section III-A, the Doppler shifts $\underline{f}_{s\breve{b}}^{\text{DA}}$ and $\underline{f}_{b\breve{s}}^{\text{UA}}$ can be computed by using (4), if we replace there β_0 by $\underline{\beta}_{s\breve{b}}^{\text{DA}}$ ($\underline{\beta}_{b\breve{s}}^{\text{UA}}$) and α_0 by $\underline{\alpha}_{s\breve{b}}^{\text{DA}}$ ($\underline{\alpha}_{b\breve{s}}^{\text{UA}}$). The expressions of the AODs $\underline{\beta}_{s\breve{b}}^{\text{DA}}$ and $\underline{\beta}_{b\breve{s}}^{\text{UA}}$ in (19) and (20) reduce to

$$\underline{\beta}_{s\breve{b}}^{\text{DA}} = \left(\breve{b} - s + \frac{3}{2}\right)\pi + (-1)^{(s-\breve{b})}\underline{\varphi}_{s\breve{b}}^{\text{DA}} \tag{32}$$

and

$$\underline{\beta}_{b\breve{s}}^{\text{UA}} = \left(b - \breve{s} + \frac{1}{2}\right)\pi - (-1)^{(b-\breve{s})}\underline{\varphi}_{b\breve{s}}^{\text{UA}} \tag{33}$$

respectively. The corresponding AOAs $\underline{\alpha}_{s\breve{b}}^{\text{DA}}$ and $\underline{\alpha}_{b\breve{s}}^{\text{UA}}$ are given by

$$\underline{\alpha}_{s\breve{b}}^{\text{DA}} = \frac{\pi}{2} + \underline{\varphi}_{s\breve{b}}^{\text{DA}} \tag{34}$$

and

$$\underline{\alpha}_{b\breve{s}}^{\mathrm{UA}} = \frac{3\pi}{2} - \underline{\varphi}_{b\breve{s}}^{\mathrm{UA}} \qquad (35)$$

respectively. By means of (30) and (31), the AOIs $\underline{\varphi}_{s\breve{b}}^{\mathrm{DA}}$ and $\underline{\varphi}_{b\breve{s}}^{\mathrm{UA}}$ can be determined as

$$\underline{\varphi}_{s\breve{b}}^{\mathrm{DA}} = \arctan\left(\frac{D}{(2s-1)y_1^T + 2\breve{b}y_2^T + y_1^R}\right) \qquad (36)$$

and

$$\underline{\varphi}_{b\breve{s}}^{\mathrm{UA}} = \arctan\left(\frac{D}{2\breve{s}y_1^T + (2b-1)y_2^T + y_2^R}\right) \qquad (37)$$

respectively. Note that the special solutions in (36) and (37) are identical with the known results in [9, Eqs. (11) and (12)].

IV. STATISTICAL PROPERTIES OF THE SOB-UWA CHANNEL MODEL

In this section, we study the statistical properties of the developed SOB-UWA channel model including the distribution of the channel envelope, instantaneous channel capacity, temporal ACF, FCF, Doppler PSD, and PDP.

A. Distribution of the Channel Envelope

Starting from the TVCIR $h(\tau', t)$, we can obtain the time-variant channel transfer function (TVCTF) $H(f', t)$ by computing the Fourier transform of the TVCIR $h(\tau', t)$ with respect to the propagation delay τ'. From (1), (2), (12), and (13), it follows that the TVCTF $H(f', t)$ can be written as

$$H(f', t) = H^{\mathrm{LOS}}(f', t) + H^{\mathrm{DA}}(f', t) + H^{\mathrm{UA}}(f', t) \qquad (38)$$

where the function $H^{\mathrm{LOS}}(f', t)$ represents the LOS part of the TVCTF $H(f', t)$, which is given by

$$H^{\mathrm{LOS}}(f', t) = c_0 e^{j\left[2\pi(f_0 t - f'\tau'_0) + \theta_0\right]}. \qquad (39)$$

The second part $H^{\mathrm{DA}}(f', t)$ and third part $H^{\mathrm{UA}}(f', t)$ of the TVCTF $H(f', t)$ can be represented as

$$H^{\mathrm{DA}}(f', t) = \sum_{s=1}^{N_S} \sum_{\breve{b}=s-1}^{s} c_{s\breve{b}}^{\mathrm{DA}} e^{j\left[2\pi(f_{s\breve{b}}^{\mathrm{DA}} t - f'\tau'^{\mathrm{DA}}_{s\breve{b}}) + \theta_{s\breve{b}}^{\mathrm{DA}}\right]} \qquad (40)$$

and

$$H^{\mathrm{UA}}(f', t) = \sum_{b=1}^{N_B} \sum_{\breve{s}=b-1}^{b} c_{b\breve{s}}^{\mathrm{UA}} e^{j\left[2\pi(f_{b\breve{s}}^{\mathrm{UA}} t - f'\tau'^{\mathrm{UA}}_{b\breve{s}}) + \theta_{b\breve{s}}^{\mathrm{UA}}\right]} \qquad (41)$$

respectively. Using the results presented in [23] regarding the statistics of the envelope of sum-of-cisoids (SOC)-based multipath fading channel models, the PDF $p_{|H|}(z)$ of the channel envelope $|H(f', t)|$ can be written as

$$p_{|H|}(z) = 4\pi^2 z \int_0^\infty \left[\prod_{n=1}^N J_0\left(2\pi|c_n|x\right)\right] J_0(2\pi z x) J_0(2\pi c_0 x) x \, dx \qquad (42)$$

where $(c_1, ..., c_N) = (c_{1,0}^{\mathrm{DA}}, c_{1,1}^{\mathrm{DA}}, c_{2,1}^{\mathrm{DA}}, c_{2,2}^{\mathrm{DA}}, ..., c_{N_S,N_S-1}^{\mathrm{DA}}, c_{N_S,N_S}^{\mathrm{DA}}, c_{1,0}^{\mathrm{UA}}, c_{1,1}^{\mathrm{UA}}, c_{2,1}^{\mathrm{UA}}, c_{2,2}^{\mathrm{UA}}, ..., c_{N_B,N_B-1}^{\mathrm{UA}}, c_{N_B,N_B}^{\mathrm{UA}})$ and $N = 2N_S + 2N_B$.

B. Distribution of the Instantaneous Channel Capacity

According to E. Telatar [24] and G. E. Shannon [25], the channel capacity $C(f', t)$ can be written as

$$C(f', t) = \log_2\left(1 + \frac{S(f')}{N(f')}|H(f', t)|^2\right) \qquad (43)$$

where f' is a tone frequency within the bandwidth of the transmit signal. In (43), $S(f')$ is the PSD of the transmit signal and $N(f')$ represents the PSD of the total underwater coloured noise component, which is given by

$$N(f') = N_t(f') + N_s(f') + N_w(f') + N_{th}(f'). \qquad (44)$$

Here, $N_t(f')$, $N_s(f')$, $N_w(f')$, and $N_{th}(f')$ are the noise PSDs resulting from the turbulence, shipping, waves, and thermal noise, respectively [26]. It should be pointed out that the noise in underwater propagation environments is strongly frequency dependent. This characteristic is usually taken into account for the selection of appropriate frequency bands for UWA communications. From (43), the instantaneous channel capacity $C(t)$ can be obtained by integrating over the frequency variable f' within the transmit bandwidth B, i.e.,

$$C(t) = \int_{f_c - \frac{B}{2}}^{f_c + \frac{B}{2}} \log_2\left(1 + \frac{S(f')}{N(f')}|H(f', t)|^2\right) df'. \qquad (45)$$

The PDF $p_C(r)$ of the instantaneous channel capacity $C(t)$ can be directly obtained from the PDF $p_{|H|}(z)$ of the channel envelope $|H(f', t)|$ in (42) by applying the concept of transformation of random variables [27, pp. 130], which results in

$$p_C(r) = \frac{2^{r-1}\log(2)}{\gamma}\sqrt{\frac{\gamma}{2^r - 1}} p_{|H|}\left(\sqrt{\frac{2^r - 1}{\gamma}}\right) \qquad (46)$$

where γ is the average signal-to-noise ratio (SNR) viewed at the receive-hydrophone side.

C. Temporal ACF, FCF, Doppler PSD, and PDP

In the following, we study the temporal ACF, FCF, Doppler PSD, and the PDP of the proposed UWA channel model. The knowledge of the TVCTF $H(f', t)$ enables us to compute the time-frequency correlation function (TFCF) of the channel. Assuming that the geometry-based SOB-UWA channel model is wide-sense stationary in time t and frequency f', we can compute the TFCF $r_{HH}(\nu', \tau)$ of the TVCTF $H(f', t)$ by using

$$r_{HH}(\nu', \tau) = E\{H^*(f', t)H(f' + \nu', t + \tau)\} \qquad (47)$$

where $(\cdot)^*$ represents the complex conjugate operation, and $E\{\cdot\}$ is the statistical expectation operator. The symbols ν' and τ denote the frequency and the time separation variables, respectively. After averaging over the random phases $\theta_{s\breve{b}}^{\mathrm{DA}}$ and $\theta_{b\breve{s}}^{\mathrm{UA}}$, the TFCF $r_{HH}(\nu', \tau)$ of the proposed UWA channel model results in (48) (see at the bottom of the next page). It should be noted that the temporal ACF $r_{HH}(\tau)$ and the FCF $r_{HH}(\nu')$ are obtained from the TFCF $r_{HH}(\nu', \tau)$ by

setting ν' and τ to zero, respectively, can be computed by (49) and (50) (see the bottom of this page). From (48), we can obtain the total power σ_{HH}^2 of the UWA channel model as $\sigma_{HH}^2 = r_{HH}(0,0)$. Moreover, the Doppler PSD $S_{HH}(f)$ can be obtained by computing the Fourier transform of the temporal ACF $r_{HH}(\tau)$ in (49) with respect to the variable τ. The PDP $S_{\tau'}(\tau')$ can be obtained by taking the inverse Fourier transform of the FCF $r_{HH}(\nu')$ in (50) with respect to the variable ν'.

D. Characteristic Quantities

The Doppler PSD $S_{HH}(f)$ enables us to compute the average Doppler shift $B_{HH}^{(1)}$, the Doppler spread $B_{HH}^{(2)}$, and the coherence time T_C of the channel. These characteristic quantities can also be expressed in closed form by using the temporal ACF $r_{HH}(\tau)$. The average Doppler shift $B_{HH}^{(1)}$ and the Doppler spread $B_{HH}^{(2)}$ are defined by the first moment and the square root of the second central moment of the Doppler PSD $S_{HH}(f)$, respectively, i.e., [28, Eqs. (3.28) and (3.29)]

$$B_{HH}^{(1)} = \frac{\int\limits_{-\infty}^{+\infty} f S_{HH}(f) df}{\int\limits_{-\infty}^{+\infty} S_{HH}(f) df} = \frac{1}{2\pi j} \cdot \left. \frac{\dot{r}_{HH}(\tau)}{r_{HH}(\tau)} \right|_{\tau=0} \qquad (51)$$

and

$$B_{HH}^{(2)} = \sqrt{\frac{\int_{-\infty}^{+\infty} \left(f - B_{HH}^{(1)}\right)^2 S_{HH}(f) df}{\int_{-\infty}^{+\infty} S_{HH}(f) df}}$$

$$= \frac{1}{2\pi} \sqrt{\left. \left(\frac{\dot{r}_{HH}(\tau)}{r_{HH}(\tau)}\right)^2 - \frac{\ddot{r}_{HH}(\tau)}{r_{HH}(\tau)} \right|_{\tau=0}}, \qquad (52)$$

where $\dot{r}_{HH}(\tau)$ and $\ddot{r}_{HH}(\tau)$ are the first and second time derivative of the temporal ACF $r_{HH}(\tau)$ with respect to the variable τ. The coherence time T_C of the channel is approximately the reciprocal of the Doppler spread $B_{HH}^{(2)}$, i.e., $T_C \approx 1/B_{HH}^{(2)}$.

Analogously, the PDP $S_{\tau'}(\tau')$ enables us to compute the average delay $B_{\tau'}^{(1)}$, the delay spread $B_{\tau'}^{(2)}$, and the coherence bandwidth B_C of the channel. These characteristic quantities can be expressed in closed form by means of the FCF. The

average delay $B_{\tau'}^{(1)}$ and the delay spread $B_{\tau'}^{(2)}$ are defined by the first moment and the square root of the second central moment of the PDP $S_{\tau'}(\tau')$, respectively, i.e., [28, Eqs. (7.39)–(7.40)]

$$B_{\tau'}^{(1)} = \frac{\int\limits_{-\infty}^{+\infty} \tau' S_{\tau'}(\tau') d\tau'}{\int\limits_{-\infty}^{+\infty} S_{\tau'}(\tau') d\tau'} = -\frac{1}{2\pi j} \cdot \left. \frac{\dot{r}_{HH}(\nu')}{r_{HH}(\nu')} \right|_{\nu'=0} \qquad (53)$$

and

$$B_{\tau'}^{(2)} = \sqrt{\frac{\int_{-\infty}^{+\infty} \left(\tau' - B_{\tau'}^{(1)}\right)^2 p_{\tau'}(\tau') d\tau'}{\int_{-\infty}^{+\infty} p_{\tau'}(\tau') d\tau'}}$$

$$= \frac{1}{2\pi} \sqrt{\left. \left(\frac{\dot{r}_{HH}(\nu')}{r_{HH}(\nu')}\right)^2 - \frac{\ddot{r}_{HH}(\nu')}{r_{HH}(\nu')} \right|_{\nu'=0}}, \qquad (54)$$

where $\dot{r}_{HH}(\nu')$ and $\ddot{r}_{HH}(\nu')$ are the first and second time derivative of the FCF $r_{HH}(\nu')$ with respect to the variable ν'. The coherence bandwidth B_C of the channel is approximately the reciprocal of the delay spread $B_{\tau'}^{(2)}$, i.e., $B_C \approx 1/B_{\tau'}^{(2)}$.

V. NUMERICAL RESULTS

In this section, we illustrate the theoretical results presented in the previous sections. One of our main objectives is to show how much the slope angle ϕ influences the statistical properties of UWA channels. Note that the ocean-bottom slope angle $\phi = -1°$ ($\phi = 1°$) results in an increase (or decrease) of the water depth of 17.4 meter per kilometer. In our simulation setup, we set the carrier frequency f_c to 10 kHz and assume that the transmitter T_x and the receiver R_x are moving at the same speed of 3 m/s, which results in maximum Doppler frequencies of 20 Hz (i.e., $f_{max}^T = f_{max}^R = 20$ Hz). The transmitter T_x and the receiver R_x are moving in opposite directions determined by $\alpha_v^T = 180°$ and $\alpha_v^R = 0°$. The T_x and R_x location parameters have been set as follows: $y_1^T = 40$ m, $y_2^T = 60$ m, $y_1^R = 15$ m, and $D = 1.6$ km. The remaining parameters of the UWA channel model are listed in the third column of Table I.

Fig. 5 displays the PDF $p_{|H|}(z)$ of the UWA channel model envelope $|H(f', t)|$ for slope angles $\phi = -3°, ..., 0°, ..., 3°$. A good fitting between theory and simulation can be observed.

$$r_{HH}(\nu', \tau) = c_0^2 e^{j2\pi(f_0\tau - \nu'\tau'_0)} + \sum_{s=1}^{N_S} \sum_{\breve{b}=s-1}^{s} [c_{s\breve{b}}^{DA}]^2 e^{j2\pi(f_{s\breve{b}}^{DA}\tau - \nu'\tau'_{s\breve{b}})} + \sum_{b=1}^{N_B} \sum_{\breve{s}=b-1}^{b} [c_{b\breve{s}}^{UA}]^2 e^{j2\pi(f_{b\breve{s}}^{UA}\tau - \nu'\tau'_{b\breve{s}})} \qquad (48)$$

$$r_{HH}(\tau) = r_{HH}(0, \tau) = c_0^2 e^{j2\pi f_0\tau} + \sum_{s=1}^{N_S} \sum_{\breve{b}=s-1}^{s} [c_{s\breve{b}}^{DA}]^2 e^{j2\pi f_{s\breve{b}}^{DA}\tau} + \sum_{b=1}^{N_B} \sum_{\breve{s}=b-1}^{b} [c_{b\breve{s}}^{UA}]^2 e^{j2\pi f_{b\breve{s}}^{UA}\tau} \qquad (49)$$

$$r_{HH}(\nu') = r_{HH}(\nu', 0) = c_0^2 e^{-j2\pi\nu'\tau'_0} + \sum_{s=1}^{N_S} \sum_{\breve{b}=s-1}^{s} [c_{s\breve{b}}^{DA}]^2 e^{-j2\pi\nu'\tau'_{s\breve{b}}} + \sum_{b=1}^{N_B} \sum_{\breve{s}=b-1}^{b} [c_{b\breve{s}}^{UA}]^2 e^{-j2\pi\nu'\tau'_{b\breve{s}}} \qquad (50)$$

Moreover, this figure shows that the average and the spread of the UWA channel model envelope distribution decrease if ϕ decreases. Fig. 6 illustrates the effect of the slope angle ϕ on the PDF $p_C(r)$ of the instantaneous capacity of the UWA channel model for an average SNR γ set to 17 dB. In fact, a relatively small decrease of ϕ results in a considerable decrease of both the average and the spread of the instantaneous capacity of the UWA channel model. For example, compared to the FOB case ($\phi = 0°$), a slope angle ϕ of -3° results approximately in an average capacity loss of 0.15 bits/s/Hz. Here again, a good agreement between the theoretical results and the corresponding simulation results can be seen.

Figs. 7 and 8 show the influence of the slope angle ϕ on the absolute value of the normalized temporal ACF $|r_{HH}(\tau)|$ and FCF $|r_{HH}(\nu')|$ of the UWA channel model, respectively. The results illustrate that both quantities decay rapidly with τ and ν' by decreasing the value of ϕ from $+3°$ to $-3°$. It can be seen from Fig. 7 that the slope angle ϕ influences significantly the curvature of the temporal ACF $|r_{HH}(\tau)|$ at the origin. From this figure we notice that the graph that corresponds to the slope angle $\phi = -3°$ descends at a faster rate than other graphs. The same results are obtained for the FCF $|r_{HH}(\nu')|$ shown in Fig. 8. As can be seen in Figs. 7 and 8, there is a good match between the theoretical results and the corresponding simulation results.

Fig. 9 depicts the Doppler PSD $S_{HH}(f)$ of the UWA channel model for the FOB case. The Doppler PSD $S_{HH}(f)$ of the UWA channel model for the SOB case has been illustrated in Fig. 10 by assuming slope angles ϕ of $+3°$ and $-3°$. From the inspection of Figs. 9 and 10, we can conclude that the path gains are influenced by the slope angle ϕ, and that its effect is also noticeable in the range of the Doppler frequencies. It is obvious that the slope angle ϕ remarkably affects the AOAs and consequently the Doppler frequencies.

Figs. 11 and 12 show the PDP $S_{\tau'}(\tau')$ of the UWA channel model for the FOB and SOB cases, respectively. Based on the results depicted in Figs. 11 and 12, the time range in the propagation delay axis is extended by decreasing the value of ϕ from $+3$ to -3. The only reason for the extension is the effect of the slope angle ϕ on increasing the total distance which each macro-eigenray travels from the transmitter to the receiver.

The effect of the slope angle ϕ on the average Doppler shift $B_{HH}^{(1)}$, Doppler spread $B_{HH}^{(2)}$, and the coherence time T_C of the UWA channel model is shown in Fig. 13. According to the results, one can conclude that the slope angle ϕ does have a considerable impact on the average Doppler shift and Doppler spread of the UWA channel model. Moreover, the coherence time T_C of the UWA channel model is almost quadrupled by increasing ϕ from $-3°$ to $3°$.

Fig. 14 shows the influence of the slope angle ϕ on the average delay $B_{\tau'}^{(1)}$, delay spread $B_{\tau'}^{(2)}$, and the coherence bandwidth B_C of the UWA channel model. It can be seen from this figure how the aforementioned characteristic functions of the UWA channel model vary w.r.t. the slope angle ϕ. According to Fig. 14, by increasing ϕ from $-3°$ to $3°$, the average delay $B_{\tau'}^{(1)}$ decreases from 25 ms to 3 ms, and also
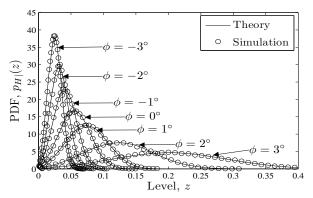

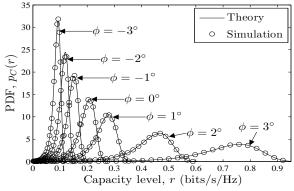Fig. 5. The PDF of the channel envelope.

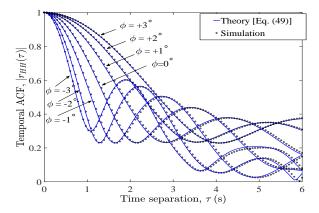Fig. 6. The PDF of the instantaneous channel capacity.

Fig. 7. Absolute value of the normalized temporal ACF $|r_{HH}(\tau)|$ of the UWA channel model.

there is a noticeable fall in the delay spread $B_{\tau'}^{(2)}$ of the UWA channel model from 22 ms to 3 ms. The coherence bandwidth B_C experiences a remarkable rise from 45 Hz to 335 Hz by increasing ϕ. For ease of reference, some parameters presented in Section III and associated values used for the computer simulations are defined in Table I.

According to the simulation results, a gradual slope in the ocean bottom changes the statistical properties of the UWA channel, thus, this parameter plays a key role in the modelling of UWA channels. Notice that the proposed UWA channel model has been studied by only considering the deterministic macro-eigenrays.

TABLE I
DEFINITION AND SELECTED VALUES OF THE CHANNEL PARAMETERS.

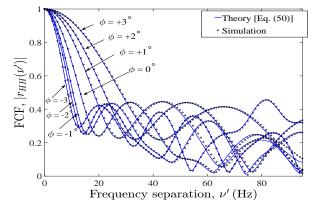| Parameters	Definitions	Figs. 5–14	Figs. 16–19
$D^{\mathrm{DA}}_{s\check{b}}$, $D^{\mathrm{UA}}_{b\check{s}}$	Total distances that the DA and UA macro-eigenrays travel from T_x to R_x	-	-
$\varphi^{\mathrm{DA}}_{s\check{b}}$, $\varphi^{\mathrm{UA}}_{b\check{s}}$	AOIs of the DA and UA macro-eigenrays at the receiver R_x	-	-
y_1^T	Distance between T_x and the ocean surface	40 m	45.5 m
y_1^R	Distance between R_x and the ocean surface	15 m	44 m
$y_1^T + y_2^T$	Water depth at the transmitter side	100 m	80 m
D	Total distance between T_x and R_x along the x-axis	1600 m	1500 m
ϕ	Ocean-bottom slope angle	Various	Fig. 16: 0° Figs. 17–18: Various Fig. 19: 0° and −0.2°
ρ_s	Density of the ocean water	1000 kg/m³	1000 kg/m³
ρ_b	Density of the ocean bed	1500 kg/m³	1500 kg/m³
c_s	Speed of sound in the ocean water	1500 m/s	1440 m/s
c_b	Speed of sound in the ocean bed	1600 m/s	1600 m/s
α_{v}^T	Angle of motion of the transmitter	180°	-
α_{v}^R	Angle of motion of the receiver	0°	-
f_c	Carrier frequency	10 kHz	17 kHz
$f_{\max}^T$	Maximum Doppler frequency associated with the transmitter T_x	20 Hz	0 Hz
$f_{\max}^R$	Maximum Doppler frequency associated with the receiver R_x	20 Hz	0 Hz
c_R	Rice factor	0.2	0.3
η_S	Ratio of the power of DA macro-eigenrays to the total power	0.5	0.5
η_B	Ratio of the power of UA macro-eigenrays to the total power	0.5	0.5
N_S	Maximum number of interactions between each DA macro-eigenray and the ocean surface	2	2 in Fig. 16, 1 in Figs. 17–19
N_B	Maximum number of interactions between each UA macro-eigenray and the ocean bottom	2	2 in Fig. 16, 1 in Figs. 17–19

Fig. 8. Absolute value of the normalized FCF $|r_{HH}(\nu')|$ of the UWA channel model.

Fig. 9. The Doppler PSD $S_{HH}(f)$ of the UWA channel model for the FOB case.

VI. COMPARISON WITH MEASUREMENT DATA

In this section, the main theoretical results presented in Sections III and IV are verified by measurement data, which was first presented in [29]. The comparison is assessed in terms of the FCF $r_{HH}(\nu')$, average delay $B_{\tau'}^{(1)}$, delay spread $B_{\tau'}^{(2)}$, and the coherence bandwidth B_C of the UWA channel.

The experimental data was collected near the New Jersey shore in May 2009 by a team from Naval Research LAB. The water depth was about 80 m and the sediment was a silty clay. The fixed transmitter was about 45.5 m below the surface float ($y_1^T = 45.5$ m). The fixed receiver hydrophone was located at 44 m depth ($y_1^R = 44$ m). The receiver was 1500 m away from the transmitter. Fig. 15 demonstrates the measurement scenario
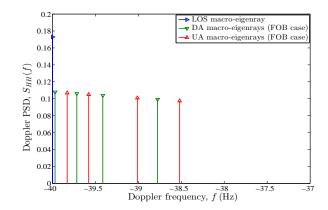
of the underwater propagation scenario. The speed of sound in that shallow water environment was about 1440 m/s and the weather was rainy and windy. The channel measurements were performed at a carrier frequency of 17 kHz and a signal bandwidth of 4 kHz. More details regarding the communication system, what was sent and received, and the type of equipment (transducer and hydrophone) can be found in [30].

We start from the measured TVCIR $\check{h}(\tau', t)$ which has been obtained by $M = 20$ samples in the time domain over a time range of $T_{\mathrm{mes}} = 8$ s. Hence, the sampling interval Δt in the time domain is $\Delta t = T_{\mathrm{mes}}/M = 0.4$ s. In the delay domain, the measurement equipment allows a path resolution of $\Delta \tau' = 0.125$ ms. The number of samples in

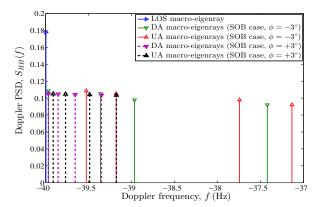Fig. 10. The Doppler PSD $S_{HH}(f)$ of the UWA channel model for the SOB case (slope angles $\phi = 3°$ and $\phi = -3°$).
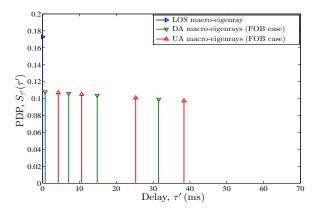

Fig. 11. The PDP $S_{\tau'}(\tau')$ of the UWA channel model for the FOB case.

the delay domain was equal to $L = 90$. In other words, the TVCIR $\check{h}(\tau', t)$ has been measured at discrete time instances $t_m = m\Delta t \in [0, T_{mes})$, $m = 0, 1, \ldots, M - 1$, and at the discrete delay interval $\tau_l' = l\Delta\tau'$, $l = 0, 1, \ldots, L - 1$. Consequently, the measured TVCIR $\check{h}(\tau', t)$ can be represented as a discrete TVCIR $\check{h}[\tau_l', t_m]$. The discrete TVCTF $\check{H}[f_q', t_m]$ can be obtained by computing the discrete Fourier transform of the TVCIR $\check{h}[\tau_l', t_m]$ with respect to delays τ_l'.
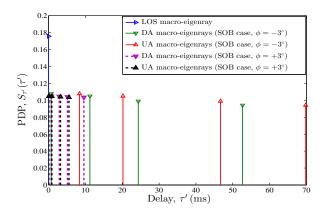

Fig. 12. The PDP $S_{\tau'}(\tau')$ of the UWA channel model or the SOB case (slope angles $\phi = 3°$ and $\phi = -3°$).
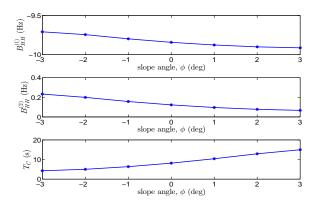

Fig. 13. The effect of the slope angle ϕ on the average Doppler shift $B_{HH}^{(1)}$, Doppler spread $B_{HH}^{(2)}$, and the coherence time T_C of the UWA channel model.
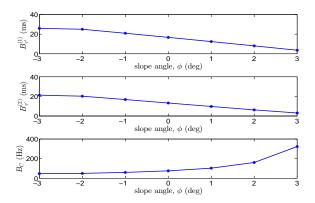

Fig. 14. The effect of the slope angle ϕ on the average delay $B_{\tau'}^{(1)}$, delay spread $B_{\tau'}^{(2)}$, and the coherence bandwidth B_C of the UWA channel model.

The discrete frequencies f_q' are given by $f_q' = -B/2 + q\Delta f' \in [-B/2, B/2]$, $q = 0, 1, \ldots, Q - 1$ and B denotes the measurement bandwidth. The discrete FCF $\check{r}_{HH}[\nu']$ can be obtained from the discrete TVCTF $\check{H}[f_q', t_m]$ as follows

$$\check{r}_{HH}[\nu'] = \frac{1}{M} \sum_{m=0}^{M-1} \check{H}[f_q', t_m] \check{H}^*[f_q' + \nu', t_m]. \qquad (55)$$

The discrete PDP $\check{S}_{\tau'}[\tau_l']$ of the measurement data can be computed by taking the inverse Fourier transform of the discrete FCF $\check{r}_{HH}[\nu']$ with respect to ν'. The average delay $\check{B}_{\tau'}^{(1)}$ and the delay spread $\check{B}_{\tau'}^{(2)}$ of the measured channel can be computed by replacing the Continuous PDP $S_{\tau'}(\tau')$ in (53) and (54), respectively, by the discrete PDP $\check{S}_{\tau'}[\tau_l']$. As mentioned in Section IV-C, the coherence bandwidth $\check{B}_c$ of the measured channel can be obtained from the channel delay spread $\check{B}_{\tau'}^{(2)}$, which is determined by $\check{B}_C \approx 1/\check{B}_{\tau'}^{(2)}$. The Rice factor c_R of the measured TVCIR $\check{h}[\tau_l', t_m]$ is obtained by using the moment method presented in [31].

In our simulation setup, we have considered nine macro-eigenrays including one LOS macro-eigenray, four DA macro-eigenrays, and four UA macro-eigenrays by assuming $N_S = N_B = 2$. Other model parameters based on the measurement scenario are defined in the forth column of Table I. Fig. 16 illustrates the PDP $\check{S}_{\tau'}[\tau_l']$ of the measured UWA channel

and that of the simulation model. Note that in case of the simulation model seen in Fig. 16, four macro-eigenrays which reach the receiver with delays of more than $10\,\mathrm{ms}$, correspond to triple- and quadruple-bounced macro-eigenrays on the surface and bottom of the ocean. Such delayed macro-eigenrays are unobserved in the measurement data. Therefore, in our simulation model, we should consider only macro-eigenrays with single and double bounces on the surface and bottom of the ocean (i.e., $N_S = N_B = 1$). With reference to Fig. 16, the number of macro-eigenrays captured from the measured UWA channel for single- and double-bounced macro-eigenrays is higher than those for the simulation model. Therefore, matching the PDP of the simulation model to that of the measured UWA channel is meaningless. For comparison purposes, we choose other statistical properties of the UWA channel, such as the FCF, average delay, delay spread, and the coherence bandwidth. Our proposed channel model has the ocean slope angle ϕ as an extra degree of freedom compared with the FOB model. This feature can help us to achieve a better fitting between our proposed UWA channel model and the measurement data w.r.t. the statistical properties of the UWA channel. To find the optimum value of the ocean slope angle ϕ, we consider the error function

$$E(\phi) = w_1 \left| \check{B}_{\tau'}^{(1)} - \tilde{B}_{\tau'}^{(1)} \right|^2 + w_2 \left| \check{B}_{\tau'}^{(2)} - \tilde{B}_{\tau'}^{(2)} \right|^2 \qquad (56)$$

where $\tilde{B}_{\tau'}^{(1)}$ ($\check{B}_{\tau'}^{(1)}$) and $\tilde{B}_{\tau'}^{(2)}$ ($\check{B}_{\tau'}^{(2)}$) denote the average delay and the delay spread of the deterministic simulation model (measured UWA channel), respectively. Note that the deterministic simulation model can be computed from the realization of a sample function of the TVCTF $H(f', t)$ of the UWA channel model presented in (38) by fixing the random phases θ_0, $\theta_{s\check{b}}^{\mathrm{DA}}$, and $\theta_{b\check{s}}^{\mathrm{UA}}$. The parameters w_1 and w_2 are weighting factors for the normalization which have been set to 0.5, i.e., $w_1 = w_2 = 0.5$. The values of other channel model parameters are listed in the fourth column of Table I. We have also considered another error function to optimize the parameter ϕ for the coherence bandwidth B_C, which is given by

$$E_{B_C}(\phi) = \left| \check{B}_C - \tilde{B}_C \right|^2 \qquad (57)$$

where $\tilde{B}_C$ ($\check{B}_C$) is the coherence bandwidth of the deterministic simulation model (measured UWA channel). From the results shown in Figs. 17 and 18, we can conclude that the minima of the error functions $E(\phi)$ and $E_{B_C}(\phi)$ are reached at $\phi = -0.2°$. As can be seen in Figs. 17 and 18, the error functions $E(\phi)$ and $E_{B_C}(\phi)$ at the slope angle $\phi = 0°$ result in 0.09×10^{-3} and 1.21, respectively.

Table II provides a comparison between the proposed channel model and the real-world UWA channel in terms of the average delay, delay spread, and the coherence bandwidth. With reference to Table II, a good agreement has been achieved between the simulation model (if $\phi = -0.2°$) and the measured UWA channel w.r.t. the aforementioned characteristic quantities. As our available measurement data was obtained in a mild SOB environment, where the slope angle ϕ was low, the obtained characteristic quantities associated with the
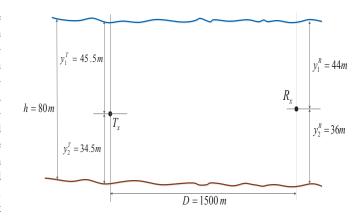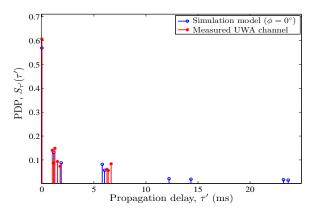

Fig. 15. The measurement scenario of the experiment.

Fig. 16. The PDP of measured UWA channel in comparison with that of the simulation model.

SOB model (with $\phi = -0.2°$) are close to those of the FOB model (with $\phi = 0°$). The superiority of the SOB case over the FOB case is more distinguishable under harsh SOB ocean conditions as discussed in Section V.

Fig. 19 illustrates the FCF of the measured UWA channel in comparison with those of the simulation model for the FOB case and the SOB case by assuming $\phi = -0.2°$. The values of the remaining channel model parameters are defined in the fourth column of Table I. As can be seen from Fig. 19, three curves are similar to each other in terms of the curvature at the origin and trend. However, the SOB case demonstrates a better performance in approximating the FCF of the measurement data. It should be mentioned that the superiority of the SOB model (over the FOB model) in approximating the FCF of the measurement data should be even more evident for ocean environments with considerable slope angles. To obtain a better fitting, we can consider clusters of micro-scatterers around macro-scatterers which results in having different eigenrays like the PDP of the measured UWA channel shown in Fig. 16. In other words, to make the proposed channel model more realistic, it should be developed by taking micro-scattering effects into account.

VII. CONCLUSION

In this paper, a new geometry-based UWA channel model has been developed under the assumption that the ocean

TABLE II
CHARACTERISTIC QUANTITIES OF THE MEASURED UWA CHANNEL AND THE CORRESPONDING SIMULATION MODEL.

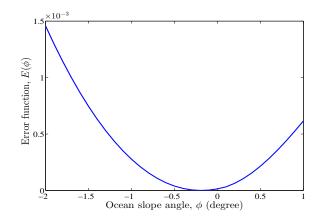| Characteristic quantities	Measured UWA channel	Simulation model ($\phi = -0.2°$)	Simulation model ($\phi = 0°$)
Average delay	$\check{B}_{\tau'}^{(1)} = 1.5$ ms	$\tilde{B}_{\tau'}^{(1)} = 1.495$ ms	$\tilde{B}_{\tau'}^{(1)} = 1.491$ ms
Delay spread	$\check{B}_{\tau'}^{(2)} = 2.4$ ms	$\tilde{B}_{\tau'}^{(2)} = 2.405$ ms	$\tilde{B}_{\tau'}^{(2)} = 2.41$ ms
Coherence bandwidth	$\check{B}_C = 416$ Hz	$\tilde{B}_C = 415.8$ Hz	$\tilde{B}_C = 414.9$ Hz

Fig. 17. Evaluation of the error function $E(\phi)$ in (56) to find the optimum value of the slope angle ϕ.
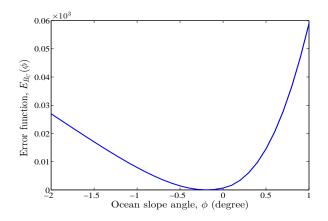

Fig. 18. Evaluation of the error function $E_{B_C}(\phi)$ in (57) to find the optimum value of the slope angle ϕ.
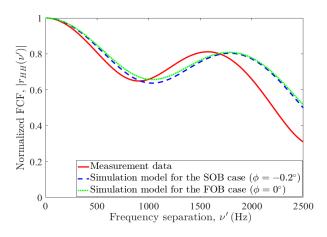

Fig. 19. The absolute value of the normalized FCF of the measured UWA channel against to those of the simulation model.

surface and bottom are smooth and also that the ocean bottom slopes gently up/down. We have studied the waveguide model in the general form by considering the SOB case. The influence of the ocean-bottom slope angle on the statistical properties of the UWA channel model has been studied. The validity of the main analytical results is confirmed by measurement data. It has been shown that the slope angle has a considerable impact on the quantities of the UWA channel and has to be considered in the area of UWA channel modelling.

ACKNOWLEDGMENT

APPENDIX

This appendix presents the proofs of (16) and (23). For brevity, we only focus on the double-bounce scattering scenario shown in Fig. 20, in which the DA macro-eigenray arrives at the transmitter R_x after a single bounce on the bottom followed by a single bounce on the surface of the ocean, i.e, $N_S = 1$, $s = 1$, and $\check{b} = 1$. According to Fig. 20, the transmitter T_x and the receiver R_x are located at the points T and R, respectively. As can be seen, the reflected macro-eigenray may be considered as emitted from the image source T_x' located at the point T' obtained by the specular reflection of the source T_x at the ocean bottom. In Fig. 20, we also observe the image source T_x'' at the point T'', which is obtained by the specular reflection of the image source T_x' at the ocean surface. The total distance that the DA macro-eigenray travels from T_x to R_x is thus equal to the side length $T''R$, which can be computed from the side lengths RI and $T''I$ by

$$T''R = \sqrt{(RI)^2 + (T''I)^2}. \quad (58)$$

Thus, we need to compute the lengths of the sides RI and $T''I$ as a function of the parameters of the geometrical channel model, namely $y_1^T, y_2^T, y_1^R, y_2^R, \phi$, and D. The length of the left side $T''I$ is $T''I = T''F + FI$, where $FI = y_1^R$ and $T''F = FT'$. The length of FT' is given by $FT' = y_1^T + ET'$, where ET' is the right side of the triangle ETT'. Thus, $ET' = TT' \cos(\phi)$, where the side TT' is the left side of the triangle $TT'B$. With $TT' = TB \cos(\phi)$ and $TB = 2y_2^T$ it then follows $ET' = 2y_2^T \cos^2(\phi)$. Now, the length of the side $T''I$ in (58) can be expressed by $T''I = y_1^T + 2y_2^T \cos^2(\phi) + y_1^R$. With reference to Fig. 20, the length of the right side RI is equal to $RG + GI$, where $RG = D$ and $GI = TE$. The side TE is given by $TE = TT' \sin(\phi)$, where $TT' = 2y_2^T \cos(\phi)$. Thus,
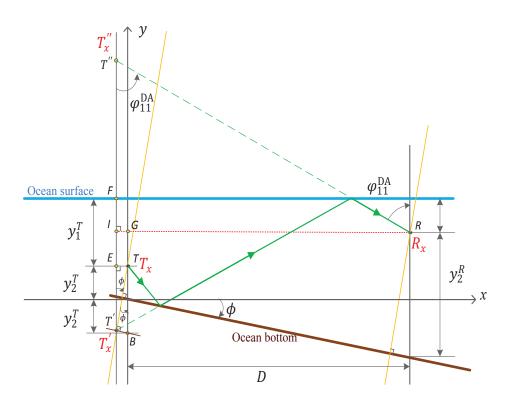
Fig. 20. Double-bounce scattering scenario for a DA macro-eigenray ($N_S = 1$, $s = 1$, and $\breve{b} = 1$).

$TE = 2y_2^T \cos(\phi) \sin(\phi)$. Now, the side RI can be obtained as $RI = D + 2y_2^T \cos(\phi) \sin(\phi)$. Finally, the total distance $T''R$ can be computed by substituting the obtained expressions for $T''I$ and RI in (58) as

$$T''R = \sqrt{(D + 2y_2^T \cos(\phi)\sin(\phi))^2 + (y_1^T + 2y_2^T \cos^2(\phi) + y_1^R)^2} . \tag{59}$$

Notice that the same results follows from (16), if we set there $s = 1$ and $\breve{b} = 1$, i.e., $D_{11}^{\mathrm{DA}} = T''R$. The AOI $\varphi_{11}^{\mathrm{DA}}$ at R_x can be computed by applying the tangent law to the triangle $T''IR$, which results in

$$\varphi_{11}^{\mathrm{DA}} = \arctan\left(\frac{D + 2y_2^T \cos(\phi)\sin(\phi)}{y_1^T + 2y_2^T \cos^2(\phi) + y_1^R}\right). \tag{60}$$

The expression above is exactly the same as the result obtained by setting $s = 1$ and $\breve{b} = 1$ in (23). Similarly, we can compute all total distances $D_{s\breve{b}}^{\mathrm{DA}}$ and $D_{b\breve{s}}^{\mathrm{UA}}$ and the corresponding AOIs $\varphi_{s\breve{b}}^{\mathrm{DA}}$ and $\varphi_{b\breve{s}}^{\mathrm{UA}}$ by using the same procedure for all values of s, $\breve{b}$, b, and $\breve{s}$. The total distances $D_{s\breve{b}}^{\mathrm{DA}}$ and $D_{b\breve{s}}^{\mathrm{UA}}$ can be computed as (61) and (62), respectively (see the bottom of this page). The functions $f^{\mathrm{DA}}(\phi)$, $g^{\mathrm{DA}}(\phi)$, and $h^{\mathrm{DA}}(\phi)$ in (61) are given

by

$$f^{\mathrm{DA}}(\phi) = \left\{ 4(s-1)y_1^T + 2\breve{b}\left[2\cos^4(\phi)\right]^{(1+s\breve{b}-s-\breve{b})} y_2^T \right\} \times \cos(\phi)\sin(\phi) \tag{63a}$$

$$g^{\mathrm{DA}}(\phi) = \left[\frac{4}{3}\cos^2(\phi) - \frac{1}{3}\right]^{(s-1)} \tag{63b}$$

$$h^{\mathrm{DA}}(\phi) = \cos^2(\phi)\left[2\cos^2(\phi) - 1\right]^{(1+s\breve{b}-s-\breve{b})} . \tag{63c}$$

The functions $f^{\mathrm{UA}}(\phi)$, $g^{\mathrm{UA}}(\phi)$, and $h^{\mathrm{UA}}(\phi)$ in (62) can be expressed by

$$f^{\mathrm{UA}}(\phi) = \left\{ 2\breve{s}\left[2\cos^2(\phi)\right]^{(1+b\breve{s}-\breve{s}-b)} y_1^T + \left[4\cos^2(\phi) + 1\right]^{(b-1)} y_2^T - y_2^R \right\} \sin(\phi) \tag{64a}$$

$$g^{\mathrm{UA}}(\phi) = \left[2\cos^2(\phi) - 1\right]^{(1+b\breve{s}-b-\breve{s})} \cos(\phi) \tag{64b}$$

$$h^{\mathrm{UA}}(\phi) = \left[\frac{4}{3}\cos^2(\phi) - \frac{1}{3}\right]^{(b-1)} \cos(\phi). \tag{64c}$$

REFERENCES

[1] A. Baptista, B. Howe, J. Freire, D. Maier, and C. T. Silva, "Scientific exploration in the era of ocean observatories," *IEEE Comput. Sci. Eng.*, vol. 10, no. 3, pp. 53–58, May 2008.

$$D_{s\breve{b}}^{\mathrm{DA}} = \sqrt{(D - f^{\mathrm{DA}}(\phi))^2 + ((2s-1)g^{\mathrm{DA}}(\phi)y_1^T + 2\breve{b}h^{\mathrm{DA}}(\phi)y_2^T + y_1^R)^2} \tag{61}$$

$$D_{b\breve{s}}^{\mathrm{UA}} = \sqrt{(D/\cos(\phi) - f^{\mathrm{UA}}(\phi))^2 + (2\breve{s}g^{\mathrm{UA}}(\phi)y_1^T + (2b-1)h^{\mathrm{UA}}(\phi)y_2^T + y_2^R\cos(\phi))^2} \tag{62}$$

[2] M. T. Rashid, A. A. Ali, R. S. Ali, L. Fortuna, M. Frasca, and M. G. Xibilia, "Wireless underwater mobile robot system based on ZigBee," in *Proc. Int. Conf. on Future Commun. Netw., ICFCN*, Apr. 2012, pp. 117–122.

[3] M. Dalbro *et al.*, "Wireless sensor networks for off-shore oil and gas installations," in *Proc. 2nd Int. Conf. on Sensor Technol. and Appl., SENSORCOMM'08*, Aug. 2008, pp. 258–263.

[4] D. Shin, S. Y. Na, J. Kim, and S. J. Baek, "Fish robots for water pollution monitoring using ubiquitous sensor networks with sonar localization," in *Proc. Int. Conf. on Convergence Informa. Technol.*, Nov. 2007, pp. 1298–1303.

[5] M. Chitre, "A high-frequency warm shallow water acoustic communications channel model and measurements," *J. Acoust. Soc. Am.*, vol. 122, no. 5, pp. 2580–2586, Nov. 2007.

[6] L. M. Brekhovskikh and Y. P. Lysanov, *Fundamentals of Ocean Acoustics*, 3rd ed.   New York: Springer, 2002.

[7] M. Stojanovic, "Underwater acoustic communications: Design considerations on the physical layer," in *Proc. Fifth Annual Conf. on Wireless on Demand Netw. Syst. and Services, WONS 2008.*, Jan. 2008, pp. 1–10.

[8] M. C. Domingo, "Overview of channel models for underwater wireless communication networks," *Physical Commun.*, vol. 1, no. 3, pp. 163 – 182, Sept. 2008.

[9] A. G. Zajić, "Statistical modeling of MIMO mobile-to-mobile underwater channels," *IEEE Trans. Veh. Technol.*, vol. 60, no. 4, pp. 1337–1351, May 2011.

[10] P. Qarabaqi and M. Stojanovic, "Statistical characterization and computationally efficient modeling of a class of underwater acoustic communication channels," *IEEE J. Ocean. Eng.*, vol. 38, no. 4, pp. 701–717, Oct. 2013.

[11] M. Naderi, M. Pätzold, and A. G. Zajić, "A geometry-based channel model for shallow underwater acoustic channels under rough surface and bottom scattering conditions," in *Proc. 5th Int. Conf. on Commun. and Electron., ICCE 2014*, Da Nang, Vietnam, July/Aug. 2014, pp. 112–117.

[12] P. Qarabaqi and M. Stojanovic, "Statistical modeling of a shallow water acoustic communication channel," in *Proc. Underwater Acoust. Meas. Conf.*, Nafplion, Greece, June 2009, pp. 1341–1350.

[13] A. Abdi and H. Guo, "Signal correlation modeling in acoustic vector sensor arrays," *IEEE Trans. Signal Process.*, vol. 57, no. 3, pp. 892–903, Mar. 2009.

[14] A. Radosevic, J. G. Proakis, and M. Stojanovic, "Statistical characterization and capacity of shallow water acoustic channels," in *Proc. IEEE OCEANS 2009 - EUROPE*, Bremen, Germany, May 2009, pp. 1–8.

[15] P. J. Bouvet and A. Loussert, "Capacity analysis of underwater acoustic MIMO communications," in *Proc. IEEE OCEANS 2010*, Sydney, Australia, May 2010, pp. 1–8.

[16] R. Hicheri, M. Pätzold, B. Talha, and N. Youssef, "A study on the distribution of the envelope and the capacity of underwater acoustic channels," in *IEEE Int. Conf. on Commun. Syst. (ICCS'14)*, Macau, China, Nov. 2014.

[17] T. C. Yang, "Toward continuous underwater acoustic communications," in *Proc. IEEE OCEANS 2008*, Quebec City, QC, Canada, Sept. 2008, pp. 1–6.

[18] ——, "A study of spatial processing gain in underwater acoustic communications," *IEEE J. Ocean. Eng.*, vol. 32, no. 3, pp. 689–709, July 2007.

[19] X. Lurton, *An Introduction to Underwater Acoustics: Principles and Applications*, 2nd ed.   Heidelberg: Springer, 2010.

[20] E. Baktash, M. J. Dehghani, M. R. F. Nasab, and M. Karimi, "Shallow water acoustic channel modeling based on analytical second order statistics for moving transmitter/receiver," *IEEE Trans. Signal Process.*, vol. 63, no. 10, pp. 2533–2545, May 2015.

[21] F. B. Jensen, W. A. Kuperman, M. B. Porter, and H. Schmidt, *Computational Ocean Acoustics*, 2nd ed.   New York: Springer, 2011.

[22] P. C. Etter, *Underwater Acoustic Modeling and Simulation*, 4th ed.   New York: CRC Press, 2013.

[23] M. Pätzold and B. Talha, "On the statistical properties of sum-of-cisoids-based mobile radio channel models," in *Proc. 10th Int. Symp. on Wireless Personal Multimedia Commun., WPMC 2007*, Jaipur, India, Dec. 2007, pp. 394–400.

[24] E. Telatar, "Capacity of multi–antenna Gaussian channels," *Bell Syst. Tech. Memo.*, pp. 379–423 and 623–656, July–Oct. 1948.

[25] C. E. Shannon, "A mathematical theory of communications," *Bell Syst. Tech. J.*, vol. 27, pp. 379–423 and 623–656, July, Oct. 1948.

[26] M. Stojanovic, "On the relationship between capacity and distance in an underwater acoustic communication channel," in *Proc. of the 1st ACM Int. Workshop on Underwater Netw. (WUWNet'06)*, Los Angeles, CA, USA, Sept. 2006.

[27] A. Papoulis, *Probability, Random Variables, and Stochastic Processes*, 4th ed.   New York: McGraw-Hill, 2002.

[28] M. Pätzold, *Mobile Fading Channels*, 2nd ed.   Chichester: John Wiley & Sons, 2011.

[29] M. Naderi, M. Pätzold, and A. G. Zajić, "The design of measurement-based underwater acoustic channel simulators using the INLSA algorithm," in *Proc. IEEE OCEANS'15*, Genova, Italy, May 2015, pp. 1–6.

[30] A. G. Zajić and G. F. Edelmann, "Feasibility study of underwater acoustic communications between buried and bottom-mounted sensor network nodes," *IEEE J. Ocean. Eng.*, vol. 38, no. 1, pp. 109–116, Jan. 2013.

[31] I. S. Greenstein, D. G. Michelson, and V. Erceg, "Moment-method estimation of the Ricean K-factor," *IEEE Commun. Lett.*, vol. 3, no. 6, pp. 175–176, Jun. 1999.

Meisam Naderi (S'13) received the B.E. degree in electrical engineering from Bahonar University of Kerman, Iran, in 2006, the M.E. degree in telecommunication engineering from Shahed University, Tehran, Iran, in 2010. He is currently working as a Ph.D. research fellow with the Department of Information and Communication Technology, University of Agder, Grimstad, Norway. His area of interests include MIMO-OFDM systems, vehicular-to-vehicular communications, underwater acoustic communications, and mobile cellular networks.

Matthias Pätzold (M'94–SM'98) received the Dipl.-Ing. and Dr.-Ing. degrees in electrical engineering from Ruhr-University Bochum, Bochum, Germany, in 1985 and 1989, respectively, and the habil. degree in communications engineering from the Technical University of Hamburg, Harburg, Germany, in 1998. From 1990 to 1992, he was with ANT Nachrichtentechnik GmbH, Backnang, Germany, where he was engaged in digital satellite communications. From 1992 to 2001, he was with the Department of Digital Networks, Technical University of Hamburg. Since 2001, he has been a full professor of mobile communications with the University of Agder, Grimstad, Norway. He is the author of several books and numerous technical papers. His publications received thirteen best paper awards. He has been actively participating in numerous conferences, serving as a member and as a chair of technical program committees. He is currently a senior editor of the IEEE Vehicular Technology Magazine.

Rym Hicheri was born in Tunis, Tunisia, in 1988. She received the D.P.C.U from the "Institut préparatoire aux études d'ingénieur d'El Manar" in 2009. She received the Eng. degree in telecommunications in 2012 from the "Ecole Supérieure des Communications de Tunis", where she is currently a Ph.D. student working under the supervision of Prof. Néji Youssef.

Néji Youssef received the B.E. degree in telecommunications from the "Ecole des Postes et des Télécommunications de Tunis", Tunisia, in 1983, and the D.E.A. in electrical engineering from the "Ecole Nationale d'Ingénieurs de Tunis", in 1986. He also received the M.E. and Ph.D. degrees in communication engineering from the University of Electro-Communications, Tokyo, Japan, in 1991 and 1994, respectively. From 1994 to 1996, he was a research associate at the University of Electro-Communications, Tokyo. Since 1997, he joined the "Ecole Supérieure des Communications de Tunis", where he is currently a professor. His research interests include noise theory, modeling of multipath fading channels and performance analysis of wireless communications.